Utrecht University
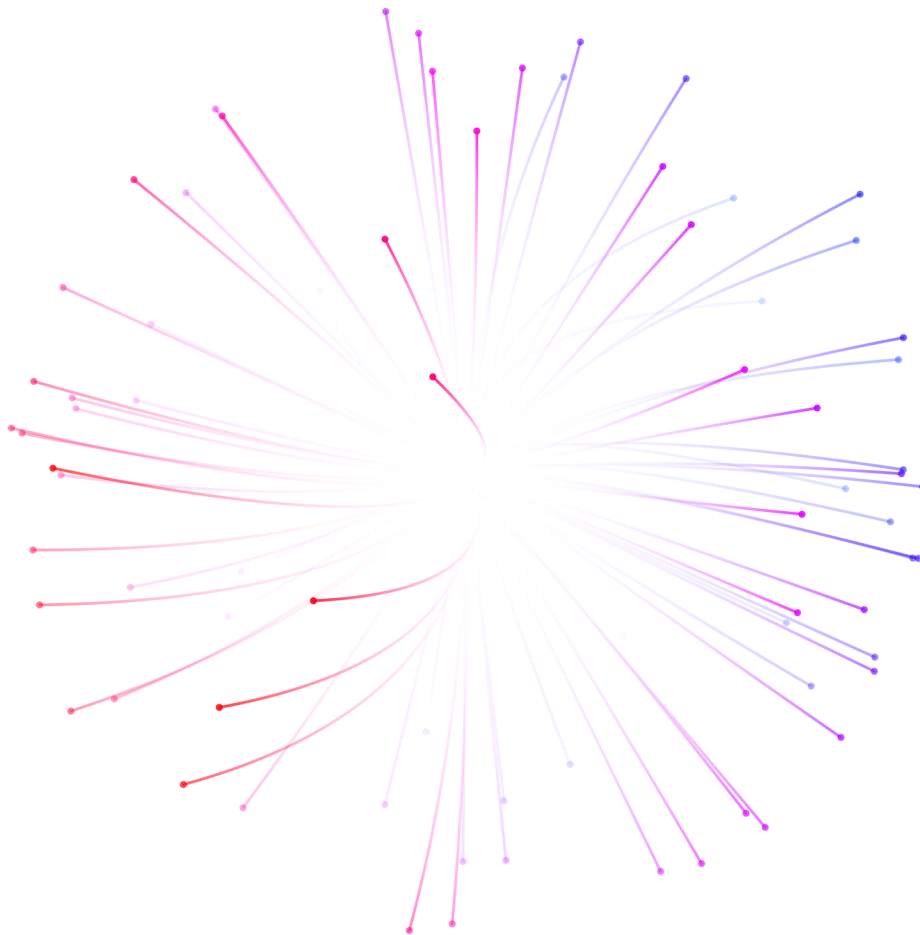
Go with the Flow
Probing the strongest magnetic field in the Universe

Bachelor's Thesis
F.A.W. Hermsen

Supervisors:

Prof. Dr. R.J.M. Snellings
Utrecht University
National Institute for Subatomic Physics (Nikhef)

Dr. A. Grelli
Utrecht University

J. Margutti MSc
Utrecht University

June 2018

Abstract

Recent studies have predicted the extreme magnitudes of the electromagnetic fields generated in non-central heavy-ion collisions, as well as the effect they may have on collision-produced charged particles in terms of directed flow. Probing these fields would improve our ability to study the simultaneously produced quark-gluon plasma, a state of matter presumed to be one of the earliest forms in which our Universe existed. In this thesis, we develop two separate toy Monte Carlo simulations in order to predict the future measurability of this directed flow. We focus on $\sqrt{s_{\mathrm{NN}}} = 5.02$ TeV $Pb + Pb$ collisions that are to take place during LHC Runs 2 & 3 at the ALICE experiment. Our results indicate that 30-50% central collisions should be most effective at demonstrating directed flow, from which discovery-level confidence could be obtained during LHC Run 3. Simplifying assumptions may impact the validity of our claims, yet they can still serve as a first-order estimation.

All figures displayed in this document have been created specifically for the purpose of this thesis.

Front page: an artist's impression of charged particles produced in non-central heavy-ion collisions while being subjected to directed flow. *The visualisation is generated by a different toy Monte Carlo simulation than those employed in our main experiment and the amount of flow is exaggerated.*

i

Contents

Acknowledgements

1 Introduction

Theoretical and experimental physics have always worked in tandem to improve our understanding of the world around us, stimulate the curiosity that is inherent to our human nature and enhance our lives in the process. As science has progressed, it has become an increasingly difficult technological enterprise to create experiments that are able to test the predictions made by the most fundamental new concepts from theoretical physics. Over the past decades, a new generation of marvels of human technological achievement such as the Laser Interferometer Gravitational-Wave Observatory (LIGO), ESA's Planck Collaboration and the Large Hadron Collider (LHC) at CERN have enabled us to probe ever deeper into the world of subatomic particles, extreme intergalactic events and the origins of the Universe itself. In this thesis, an attempt will be made at making an (infinitesimally small) contribution to this relentless march that is the progress of science.

In the currently prevailing models describing the beginning of our Universe, it is hypothesised that mere moments after the Big Bang (t $< 10^{-6}$ s) the Universe was so extremely hot and dense that quarks and gluons, the strongly interacting constituent particles of hadrons and their related force carriers, were still deconfined due to asymptotic freedom and could move around relatively freely (see Fig. 1). As a consequence, the Universe at this time is thought to have been filled with a state of matter best described as a hot, dense, ultrarelativistic quark-gluon plasma (QGP) [1, 2]. The extreme energy densities required to form such a QGP exceed anything we observe in our present Universe by several orders of magnitude. Needless to say, studying the properties of the QGP has long been an impossible task.

With the advent of the Relativistic Heavy Ion Collider (RHIC) and more recently the LHC however, we are finally able to reproduce these conditions and create QGP's for a very short period of time (t ~ 10 fm/c) in so-called heavy-ion collisions (HIC's). At the LHC for instance, beams of lead (Pb-208) nuclei are accelerated in opposing directions toward velocities extraordinarily close to the speed of light before being collided with per-nucleus energies in the order of several TeV's. This temporarily creates the conditions required for the formation of a quark-gluon plasma [3], which then can be studied by state-of-the-art instruments such as the ALICE detector (A Large Ion Collider Experiment).

Studying the QGP directly is impossible because of its short lifespan. As it expands and cools off however, its constituents form a plethora of high-momentum hadrons that can be registered in the ALICE detector and of which the collective properties provide us with information about the QGP from which they originate [4]. Of these hadrons, mesons containing heavy-flavour quarks are of special interest because due to their mass, their constituent quarks form earlier than the other components of the QGP and can therefore effectively serve as probes of the plasma as they traverse it [5].
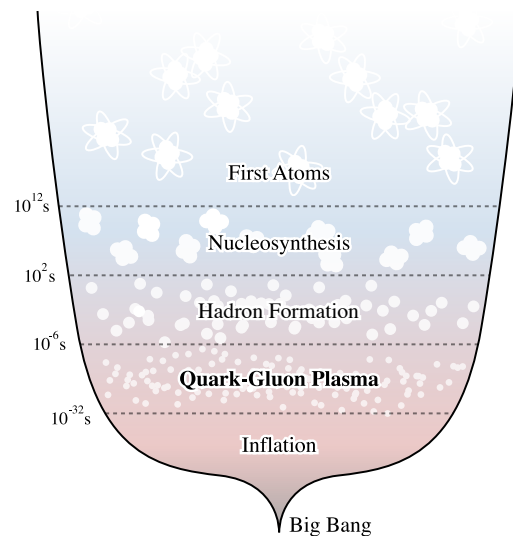

Figure 1: A schematic representation of the evolution of the early Universe.

One topic of current interest are the extreme electromagnetic fields that theory predicts to exist shortly after these collisions if they are sufficiently non-central. Since the previously mentioned heavy-flavour quarks are charged particles, the EM fields should influence their trajectories, resulting in a distinct anisotropy in their collective spatial distributions when they reach the detector in the form of mesons [6]. Because the heavy-flavour quarks would traverse the QGP while being deflected, we might in turn infer properties of the QGP from studying this anisotropy and test predictions from quantum chromodynamics (QCD). The following sections elaborate on how this expected anisotropy can be expressed as a single measurable in the form of the directed-flow parameter v_1.

In this thesis, we employ several toy Monte Carlo simulations in order to give an estimate of the level of significance to which the existence of these electromagnetic fields could be demonstrated through the measurement of v_1 from ALICE data after LHC Run 3[1] (1), which centrality class will be most effective in discerning this effect (2) and to which level of precision we might be able to reconstruct the magnitude of v_1 (3).

---

[1] According to CERN's Medium-Term Plan for the period 2018-2022, Run 3 of the LHC will take place from 2021 to 2023 after a two year long shutdown (LS2) [7].

2 Background

The following subsections briefly review the concepts from physics relevant to our toy Monte Carlo simulations. Sections 2.1 and 2.3 concerning quarks, the QGP and collision kinematics, present several concepts and equations from the relevant fields of theory, often without further proof or reference as most of them belong to the canon of modern physics. The content of these sections is well described in *Subatomic Physics* by Henly & Garcia [8]. Another, slightly less theoretical work (aimed at the undergraduate level) is *Nuclear and Particle Physics* by Martin [9].

2.1 Quarks and the QGP

The modern-day framework for describing particle physics is the Standard Model. It is a gauge quantum field theory that encompasses three of the four fundamental forces (the strong, weak and electromagnetic interactions) as well as a classification of elementary particles. In this model, nucleons are no longer seen as the fundamental building blocks of matter: they are composite particles, consisting of three quarks held together by the strong force (confinement). Experiments in the 1970's have already confirmed the existence of these quarks, of which the electric charges are either $\pm\frac{1}{3}$e or $\pm\frac{2}{3}$e. How these quarks interact with one another through the strong force and its force carriers, gluons, is described by the theory of quantum chromodynamics (QCD), a non-commutative quantum field theory with symmetry group SU(3). An overview of the six quark flavours currently described in the Standard Model and their relevant properties can be found in Table 1.

Nucleons are just some of the composite particles consisting of confined quarks. All bound quark states fall under the umbrella of hadrons, which in turn can be split into two distinctly different families: baryons and mesons. Baryons are bound states of three quarks (or three antiquarks) and belong to the family of fermions (particles with odd half-integer spin). Mesons are bound states of one quark and one antiquark, belonging to the family of bosons (particles with integer spin)[2].

As previously mentioned, quarks are confined by means of the strong force under the circumstances usually witnessed in our present Universe. From pertubative QCD, it can be shown that the coupling constant of the strong force, the measure of its strength, is approximately described by

$$\alpha_s = \frac{12\pi}{(33 - 2N_f)\ln{(Q^2/\Lambda^2)}}, \qquad (1)$$

in which N_f is the number of quark flavours existing in QCD (six, as displayed in Table 1), Λ is an experimental scale parameter determined at 0.2 ± 0.1 GeV/c and Q^2 is the squared four-momentum transfer, which grows as the energy E_q increases, but also as the distance r decreases. Going back to (1), this entails that at common energy levels, quarks experience little to no coupling if they are sufficiently close together but start to attract one another strongly once they approach $r \sim R_{\text{proton}}$, leading to the previously mentioned confinement within that distance. If E_q becomes sufficiently large however, this effective confinement distance increases accordingly until the quarks become virtually unboud altogether. This decrease in coupling as E_q increases or r decreases, is called asymptotic freedom[3]. The name refers to the logarithmic nature of the running coupling constant fall-off.

Predictions from QCD suggest that at energy densities of ~ 1 GeV/fm^3 (or $k_B T \sim 170$ MeV) quarks become sufficiently deconfined for the formation of a QGP, the state in which the quarks and gluons move around freely enough to be treated as a fluid. In the ALICE detector, $Pb + Pb$ collisions occur with a total per-nucleus, center-of-mass energy $\sqrt{s_{NN}} = 2.76$ TeV and 5.02 TeV, leading to the creation of a fireball with an energy density in excess of 10 GeV/fm^3 at the point of collision, well over the required threshold [11]. At this stage, we might even consider only gluon degrees of freedom in the form a hypothetical gluon plasma (a *glasma*), formulable within classical Yang–Mills theory [12]. Shortly after the collision, the extremely high energy density leads to the conversion of some of the gluons to quark-antiquark pairs, forming the QGP [13][4]. Finally, the QGP ceases to exist when after hydrodynamic expansion the energy density drops below the deconfinement threshold and the QGP quarks become reconfined (hadron freeze-out).

2.2 Charm quarks and D mesons

From an energy conservation standpoint, the masses of the quark-antiquark pairs that can be produced in collisions are limited by the energy budget available. This means that heavy-flavour quarks (second generation or higher, see Table 1) can only be created in the primordial stage of the collision, when the energy density is sufficient. The relation most often used is a formation time $\tau_q \sim 1/2M_q$.

---

[2]The numbers of bound quarks mentioned only take the *valence* quarks into account: the quarks that give rise to the properties of their parent hadrons. Within hadrons however, *sea* quarks also exist, postulated to arise from vacuum fluctuations and gluons splitting into quark-antiquark pairs. They create small background fluctuations that are negligible within the context of this thesis.

[3]In drawing these conclusions we assume $N_f = 6$, which is the case for present QCD.

[4]Quarks are always created in tandem with their antiquark siblings due to QCD considerations, or more simply put: conservation laws concerning their quantum numbers [8, 9].

Name	Symbol	Mass (MeV/c²)	J	B	Q (e)	I₃	C	S	T	B'	q̄
First Generation											
Up	u	$2.2^{+0.6}_{-0.4}$	$^1/_2$	$+^1/_3$	$+^2/_3$	$+^1/_3$	0	0	0	0	$\bar{u}$
Down	d	$4.7^{+0.5}_{-0.4}$	$^1/_2$	$+^1/_3$	$-^1/_3$	$-^1/_3$	0	0	0	0	$\bar{d}$
Second Generation											
Charm	c	$1.28^{+0.03}_{-0.03} \times 10^3$	$^1/_2$	$+^1/_3$	$+^2/_3$	0	+1	0	0	0	$\bar{c}$
Strange	s	96^{+8}_{-4}	$^1/_2$	$+^1/_3$	$-^1/_3$	0	0	-1	0	0	$\bar{s}$
Third Generation											
Top	t	$173.1^{+0.6}_{-0.6} \times 10^3$	$^1/_2$	$+^1/_3$	$+^2/_3$	0	0	0	+1	0	$\bar{t}$
Bottom	b	$4.18^{+0.04}_{-0.03} \times 10^3$	$^1/_2$	$+^1/_3$	$-^1/_3$	0	0	0	0	-1	$\bar{b}$

Table 1: Quarks and their properties [10]. For the purposes of this thesis, the mass and electric charge Q are most relevant. Also listed are the quantum numbers J (total angular momentum), B (baryon number), I_3 (isospin), C (charm), S (strangeness), T (topness) and B' (bottomness). All quantum numbers (including charge Q) change sign for their antiquark counterparts, with the exception of spin J.

For charm quarks (CQ's), this entails $\tau_c \sim 0.1$ fm/c, whereas the less massive QGP constituents form only after ~ 1 fm/c. Furthermore, the kinetic relaxation time of CQ's (via the inverse of the drag coefficient $\tau_c^{eq} \simeq 1/\Gamma$)[5] is estimated to be 5 - 8 fm/c, which is comparable to the QGP lifetime [5], although other sources suspect a slightly shorter 4 - 6 fm/c [14]. This is mostly because different theoretical approaches yield different values for Γ.

Because of their early formation and relatively long relaxation time, CQ's can serve as excellent probes of the QGP since they traverse it before becoming mesons during the hadron freeze-out. We can study the resulting meson populations containing these CQ's, mainly D mesons [15][6], and compare them to the D-meson populations generated in proton-proton collisions of the same $\sqrt{s_{NN}}$. Because the $p + p$ collisions do not generate the required energy density to form a QGP, we can attempt to infer properties of the plasma, such as its viscosity and electromagnetic conductivity, by comparing these obtained populations. An overview of the relevant D mesons detected by ALICE can be found in Table 2.

The detection of D mesons is not straightforward since they decay before reaching the detectors, due to their short mean lifetime. They can however be reconstructed by analysing their decay products: kaons, pions and ϕ mesons. The decay channels generally exploited for reconstruction (including their branching ratio) in ALICE are [16]:

$D^0 \rightarrow K^+\pi^-$ (3.9%)
$D^+ \rightarrow K^-\pi^+\pi^-$ (9.5%)
$D^{*+} \rightarrow D^0\pi^+$ (68%)
$D_s^+ \rightarrow \phi\pi^+ \rightarrow K^+K^-\pi^+$ (2.3%)

The D-meson reconstruction by means of these decay channels is possible via geometric vertex reconstuction based on momentum conservation. For instance, a detected pair of K^+ and π^- may have trajectories that lead back to the same point in spacetime (secondary vertex), indicating that they might be decay products of the same D^0 parent. Momentum conservation at the decay spacetime location enables us to retrieve the original D^0 momentum, which is illustrated in Fig. 2. How well this trajectory points at the primary vertex (reconstructed point of collision) can be expressed as the pointing angle $\theta_{pointing}$ (for D^0 selection, $\cos\theta > 0.95 - 0.98$ is required). Reconstructed distances of closest approach between the decay products and the primary vertex (impact parameters d_0) serve as an extra selection criterum in order to reject decay products that are more likely to be primary collision products [15].

The decay channel branching ratios clearly show that only a relatively small portion of all D mesons produced in the collisions will make it into the final data sample. Additionally, more statistics are lost because the mesons need to be distinguished from an omnipresent, non-negligible background signal. This means that statistical cuts have to be performed to the gaussian distributions of suspected D mesons ($\pm 3\sigma$ is common, leading to another $\sim 5\%$ signal reduction [17]).

A final complicating matter arises due to bottom quarks, of which a sizable population is also produced in the collisions. Many of them are confined in B mesons after hadron freeze-out, of which a large fraction decays into the various D-meson species [10]. These are characterised as feed-down D mesons, as opposed to prompt D mesons originating from QGP charm quarks. A significant por-

---

[5]This relation holds in the momentum limit $p_c \rightarrow 0$, but τ_c^{eq} will only increase for higher p_c [14].
[6]We shall ignore the production of charmed lambda baryons $\Lambda_c^\pm$ with a relevant abundancy of $\sim 8\%$ for the purpose of this thesis.

Meson	Antiparticle	Quark Content	Mass (MeV/c^2)	Mean Lifetime (μm/c)
D$^+$	D$^-$	c$\bar{\text{d}}$	1869.59 ± 0.09	312 ± 2
D^0	$\overline{\text{D}}^0$	c$\bar{\text{u}}$	1864.83 ± 0.05	122.9 ± 0.5
D$_s^+$	D$_s^-$	c$\bar{\text{s}}$	1968.28 ± 0.10	150 ± 2
D^{*+}	D^{*-}	c$\bar{\text{d}}$	2010.26 ± 0.05	$\sim 2.4 \times 10^{-6}$
D^{*0}	$\overline{\text{D}}^{*0}$	c$\bar{\text{u}}$	2006.85 ± 0.059	$> 1 \times 10^{-7}$

Table 2: D mesons detected by ALICE in $p + p$ and $Pb + Pb$ collisions and their relevant properties [10]. The antiparticle counterparts of the mesons contain the antiquark counterparts of their constituent quarks. The same quark content can be found in different mesons, this is due to spin (anti-)alignment. D* mesons (vector) are highly unstable states and decay into other D mesons (pseudoscalar) [8]. Their mean lifetime values are computed using their resonance width via $\tau = \hbar/\Gamma$.
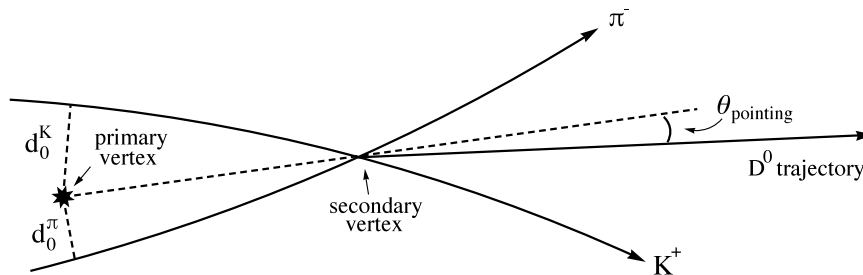

Figure 2: The topology of D^0 decay including impact parameters d_0 and pointing angle θ_{pointing}. The D^0 trajectory can be reconstructed from the K$^+$ and π^- measurements [15].

tion of these can be rejected based on vertex reconstruction techniques, but still a data sample pollution of $\sim 10\%$ remains [18]. This weakens our ability to characterise the prompt D-meson populations to some extent, but will be disregarded within the scope of this thesis for simplicity purposes.

As this thesis does not concern a detector simulation, we shall omit a detailed characterisation of the different types of charged particle detectors implemented in ALICE as well as description of the detector physics. A comprehensive overview can be found in [15].

2.3   Collision Kinematics

In order to develop a parameter framework for our simulations, let us now briefly discuss the relevant collision kinematics. We shall adopt a cartesian coordinate system of which the origin is located at the point of collision and the z-axis is aligned with the incoming particle beams. The choice of direction for the x and y-axes is not crucial due to symmetry considerations. We shall adopt the convention in which the xz-plane is aligned with the plane of the circular acceleration trajectory.

Heavy-ion collisions are rarely perfectly central: they are stochastic processes similar to classical random collisions of spherical objects, with the exception that their pre-collision momenta are virtually perfectly parrallel due to the nature of the acceler-

ation process. The distance between the parrallel momentum axes is defined as the impact parameter b. A schematic overview of a non-central collision ($b > 0$) can be seen in Fig. 3. Geometric properties of the collision are mainly determined by the impact parameter [19]. This includes the number of collision-participating nucleons N_{part} (black disks in Fig. 3), the number of spectating nucleons N_{spec} (white circles) and the number of average binary (nucleon-nucleon) collisions N_{coll}. Spectator nucleons do not participate in the collision and continue along the beam direction, leading to a smaller multiplicity of produced particles for higher impact parameters. The average values of these quantities have been calculated in great detail through Glauber Monte Carlo simulations for the relevant $Pb + Pb$ collisions, from which also the more commonly used centrality classes follow (defined as intervals between 0-100%, with 0% being most central and 100% most peripheral) [19].

In addition to the previously defined coordinate system, we define the reaction plane (RP): a rotation of the xy-plane with angle Ψ_{RP} such that the impact parameter vector $\vec{b}$ points through the x'-axis and both Pb trajectories lie in the $x'z$-plane [15]. The resulting $x'y'z$ coordinate system is unique for every collision event and is relevant to the final particle trajectory distributions. Ψ_{RP} can be reconstructed from a combination of multi-particle correlations in the azimuthal angle distribution and
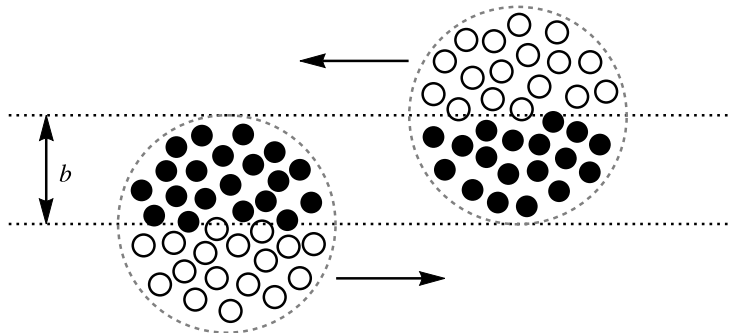
Figure 3: A schematic representation of a non-central heavy-ion collision including the impact parameter b. The collision-participating nucleons are displayed as black disks. Note that due to ultrarelativistic length contraction, the nuclei are flattened to about the width of a nucleon in the CM frame.

the elliptic flow (more in Section 2.4). Because Ψ_{RP} is initally unknow, the azimuthal angle ϕ of detected particles are measured in the original xy-plane.

As LHC collision physics take place in the ultrarelativistic regime, it is convenient to perform calculations in four-dimensional spacetime. The most common way of denoting collision energies is the center-of-momentum energy E_{cm}, which is given by

$$E_{\mathrm{cm}}^2 \equiv s = p_\mu p^\mu,$$
$$= (E_1 + E_2)^2 - (\mathbf{p}_1 + \mathbf{p}_2)^2, \quad (2)$$

in which p denotes the four-momenta of the colliding particles and $\mathbf{p}$ represents the familiar three-dimensional momenta. $\sqrt{s}$ is a Lorentz-invariant quantity in which LHC $p + p$ collision energies are usually reported. The center-of-momentum energies of heavy-ion collisions are appropriately scaled by their number of nucleons in the form of the per-nucleon-pair energy $\sqrt{s_{\mathrm{NN}}}$.

The charged particles produced in the LHC experience considerable boosting along the z-direction, which makes the momentum component parrallel to the z-axis p_{L} (longitudinal) an inconvenient measure. This problem can be circumvented by using the definition of rapidity y (relative to the z-axis),

$$y = \frac{1}{2} \ln \frac{E + p_{\mathrm{L}} c}{E - p_{\mathrm{L}} c}, \quad (3)$$

which is an additive quantity. For $m \ll p/c$, which is the case for collision products at LHC energies, $E \approx |\mathbf{p}|$, which enables us to define a pseudorapidity η:

$$\eta = \frac{1}{2} \ln \frac{|\mathbf{p}| + p_{\mathrm{L}}}{|\mathbf{p}| - p_{\mathrm{L}}},$$
$$= -\ln \left[\tan \left(\frac{\theta}{2} \right) \right], \quad (4)$$

in which θ is the angle relative to the beam in the CM frame. Together, η and ϕ give a complete description of the direction of a particle and the magnitude of p_{L}. The missing component is the momentum in the transverse direction p_{T}. This quantity is not subject to boosting, however, and can also be measured directly.

2.4 Anisotropic Flow

The collective azimuthal angle distribution of charged particle production in heavy-ion collisions is generally found not to be uniform. There is a multitude of conceivable mechanisms that could lead to this phenomenon called anisotropic flow. It is commonly studied by means of a Fourier Series expansion of the particle ϕ-distributions:

$$\frac{d^2 N}{d\eta\, d\phi} = \frac{dN}{d\eta} \left(1 + \sum_{n=1}^{\infty} 2v_n(\eta) \cos(n[\phi - \Psi_{\mathrm{RP}}]) \right) \quad (5)$$

in which the coefficients v_n tend to depend on the rapidity η and transverse momentum p_{T} [20, 21]. The directed flow, which is the main focus of our experiment, is characterised by the first coefficient $v_1(\eta)$. The elliptic flow (v_2) and triangular flow (v_3) are also of great interest but fall outside the scope of this thesis. Elliptic flow, for instance, can be employed to estimate the QGP viscosity and reconstruct the reaction-plane angle, which is then commonly denoted by Ψ_{EP} (event-plane angle) [21][7].

---

[7]To be more precise, Ψ_{EP} is not exactly the same as Ψ_{RP}. Participating nucleons are not isotropically distributed within the collision overlap region, leading to a participant-plane angle Ψ_{PP} which fluctuates around Ψ_{RP}. This means that Ψ_{EP} is actually the reconstructed value of Ψ_{PP} in this case, because it largely depends on the initial geometry of the collision participants [22].

In recent years, it has been postulated that due to the continued movement of the spectator nucleons along the beam direction in non-central heavy-ion collisions, a very strong magnetic field is created around the time of collision and during the development of the QGP [5]. The estimated initial field strengths are in the order of 50 m_π^2/e, which is far stronger than anything we encounter in our observable Universe. This could result in a charge-dependent vorticity in the reaction plane in the form of directed flow [6].

Due to the high spectator velocity, the magnetic field strength $|\vec{B}| = B_{y'}$ (perpendicular to the reaction plane) would be strongly time-dependent. This leads to a charge-dependent induced electric current inside the QGP due to Faraday's law (J_{Faraday}). The QGP, however, also undergoes a rapid initial expansion along the z-axis, resulting in a Lorentz boost of which the magnitude depends on the spacetime location within the QGP. As a consequence, some of the $\vec{B}$ field is converted into an $\vec{E}$ field, leading to a charge-dependent current perpendicular to $\vec{B}$ and z, opposite to J_{Faraday}. Due to similarities with the classical Hall effect, this current will be denoted by J_{Hall} [6]. The emerging directed flow is due to the remaining current after their partial cancellation (see Fig. 4).
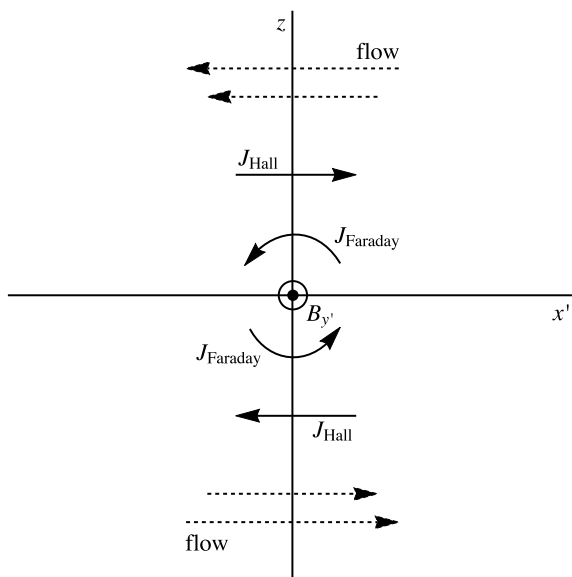

Figure 4:   A schematic representation of the (spacetime-dependent) induced magnetic field $B_{y'}$ due to spectator movement, the resulting currents due to Faraday and Hall effects and the resulting directed flow for positively charged particles. $J_{\text{Hall}} > J_{\text{Faraday}}$ in the case shown [6]. The QGP undergoes expansion in the $\pm z$-direction.

Whether the $\vec{E}$ or $\vec{B}$ field is stronger, depends entirely on the location in spacetime. Furthermore, the manner in which a particle responds to the fields depends heavily on its momentum. In case we assume that the induced velocities are non-relativistic relative to the local QGP, this is given by

$$m(\frac{d\vec{v'}}{dt} + \Gamma\vec{v'}) = q\vec{v'} \times \vec{B'} + q\vec{E'},   \quad (6)$$

in which Γ is the QGP drag coefficient and the accents indicate the boosted-particle frame of reference. The resulting flow in the collective particle distribution can therefore only be obtained through an integration over all of spacetime, weighted by the QGP spacetime evolution and the charged particle momentum distributions.

Computing just the spacetime-dependent $\vec{E}$ and $\vec{B}$ fields is already a complicated procedure. Recent efforts have provided analytical solutions to Maxwell's equations in this situation (which wil not be presented in this thesis), yet only under the assumption of a constant QGP electromagnetic conductivity σ_{el}. This is not entirely realistic since σ_{el} should be T-dependent and decrease as the plasma expands, yet it has provided us with a first-order estimation of the magnitude of the integrated directed flow [6].

The remaining integrations over the QGP spacetime evolution and particle momentum distributions have to be calculated numerically. In a 2017 study, this has been performed specifically for charm-quark production in $\sqrt{s_{\text{NN}}} = 2.76$ TeV $Pb + Pb$ collisions under the assumption of a constant QGP electromagnetic conductivity of $\sigma_{el} = 0.023$ fm^{-1} and an impact parameter of $b = 9.5$ fm [5]. The resulting directed-flow coefficient for D mesons, integrated over spacetime and the CQ momentum distributions was computed to be

$$\frac{dv_1}{d\eta}\bigg|_{\eta=0} \simeq \pm 1.75 \times 10^{-2},   \quad (7)$$

depending on the CQ charge. For $-1 < \eta < 1$, which is the relevant rapidity range for the ALICE detector [15], this relation is effectively linear and remains approximately constant within the relevant time scale (the dynamics were studied up to $t = 12$ fm/c). In this case, the Hall effect was found to be dominant over the Faraday effect.

It is important to note that a non-negligible directed flow could also be generated by other physics phenomena, such as a general vorticity due to the initial angular momentum of the QGP [23]. This component of the directed flow however, would not be odd in electric charge. This means that the flow due to the EM fields should be distinguishable from other flow effects through comparison of the charm and anticharm D-meson populations [6]. We therefore disregard other potential sources of directed flow for the remainder of this thesis in order to obtain more tractable simulation conditions.

3 Methodology

In this thesis, we develop two separate toy Monte Carlo simulations designed to predict the measurability of the v_1 directed-flow parameter as presented in Eq. 7. From this point forward, these wil be denoted as SIM1 and SIM2. They are performed in the environment of CERN's own ROOT Data Analysis Framework (6.10.8) and make use of the AliFlow package from AliPhysics [24].

We simulate different numbers of $Pb+Pb$ events in three separate centrality classes (10-30%, 30-50%, 60-80%) and investigate the improvement of the statistics. The collision energy is set at $\sqrt{s_{\mathrm{NN}}} = 5.02$ TeV, compatible with ALICE data from LHC Runs 2 & 3. The following subsections describe the scope of the simulations, after which motivations for the parameter choices are presented.

3.1 SIM1

SIM1 generates collisions on an event-by-event basis. D mesons are generated according to an initial transverse momentum (p_{T}) distribution. Based on their received p_{T} value, particles are either rejected or accepted into the final dataset through a chance process based on actual ALICE detector efficiency and acceptance properties. The simulation code is a modification of and an expansion on the `runFlowAnalysisOnTheFly` macro from the AliFlow package [25]. The parent classes `AliFlowEventSimpleMakerOnTheFly` and `AliFlowAnalysisWithMCEventPlane` were also modified to comply with the requirements from the relevant physics. For an overview of the modifications, we refer to GitHub [26] and Appendix A.

The following parameters are generated for each collision event: the reaction-plane angle (Ψ_{RP}) and the error on said reaction-plane angle ($\epsilon_{\Psi\mathrm{RP}}$). The following parameters are generated for each D meson: charge (Q), pseudorapidity (η), transverse momentum (p_{T}) and azimuthal angle (ϕ). The total statistics of SIM1 are determined by the number of collision events simulated (N_{events}) and the per-event multiplicity of prompt D mesons ($M_{\mathrm{D,prompt}}$) depending on the centrality class.

3.2 SIM2

SIM2 disregards both the particle p_{T} as well as the detector acceptance $\times$ efficiency profiles: it simulates only the prompt D mesons that will make it into the final dataset (raw prompt D-meson yield $N_{\mathrm{D,prompt}}^{\mathrm{RAW}}$). This is a simplification that is justified for a value of v_1 that is p_{T}-integrated (see Section 2.4). Even though SIM2 lacks more extensive information about the collision data (such as raw p_{T} spectra), the simplification reduces the simulation runtime by a factor ~ 10. This enables us to simulate a large range of different $N_{\mathrm{D,prompt}}^{\mathrm{RAW}}$ and

describe the improvement of the statistics quantitatively. SIM2 is a custom-made build, although it draws upon methods used in SIM1. See [27] for the complete source code.

The individual prompt D mesons are simulated without any parent event. We generate Q, η, ϕ and $\epsilon_{\phi\mathrm{RP}}$ (as if received from a hypothetical parent collision event) on a per-particle basis. The total statistics are determined directly by the raw prompt D-meson yields $N_{\mathrm{D,prompt}}^{\mathrm{RAW}}$.

3.3 The Reaction Plane

In this and subsequent sections, distribution functions do not contain normalisation constants.

Due to the stochastic nature of collision dynamics, we should not expect any anisotropy in the Ψ_{RP} distribution, which allows us to set a uniform, random distribution function that obeys

$$\frac{dN_{\mathrm{events}}}{d\Psi_{\mathrm{RP}}} = 1, \quad \Psi_{\mathrm{RP}} \in [0, 2\pi). \tag{8}$$

Ψ_{RP} can only be determined to within an uncertainty of $\sim 10\%$ for the 10-30% and 30-50% centrality classes and $\sim 15\%$ for 60-80% due to $\Psi_{\mathrm{RP}} - \Psi_{\mathrm{PP}}$ misalignment [28]. If we assume that this uncertainty displays a Gaussian behaviour, we can incorporate this by generating an error randomly via

$$f(\epsilon_{\Psi\mathrm{RP}}) = e^{-\frac{\epsilon_{\Psi\mathrm{RP}}^2}{2/25\pi^2}}, \tag{9}$$

in case of a 10% uncertainty (out of 2π). A consequence of the application of this randomised error is the introduction of both an extra uncertainty as well as a systematic bias in the measurement of v_1, as it depends on the value of Ψ_{RP}. The true value of v_1 can be obtained from the measured value v_1' via the correction

$$v_1 = \frac{v_1'}{\langle \cos(\epsilon_{\Psi\mathrm{RP}}) \rangle}. \tag{10}$$

We determine these correction factors to machine precision through numerical integration at $\langle \cos(\epsilon_{\Psi\mathrm{RP}}) \rangle = 0.8208$ (10-30% and 30-50% centrality) and 0.6414 (60-80% centrality). The results reported in Section 4 have been corrected accordingly.

3.4 Charge

As previously discussed, the CQ's are initially formed in charm-anticharm pairs. We therefore assume $N_{\mathrm{c}} = N_{\bar{\mathrm{c}}}$ and randomly tag D mesons as either $+1$ or -1 in order to generate two different D-meson populations (containing either c or $\bar{\mathrm{c}}$).

3.5 Pseudorapidity

Previous studies have shown that the charged particles produced in $Pb+Pb$-collisions, do not obey a uniform rapidity distribution [29]. They show signs of a double-Gaussian distribution with a slight decrease around mid-rapidity. For $-1 < \eta < 1$ (the domain relevant to our simulation), this can be approximated by a quadratic function. We perform weighted fits to $\sqrt{s_{\mathrm{NN}}} = 5.02$ TeV ALICE $Pb + Pb$ data presented in [29] with the function $f(\eta) = a + b\eta^2$. The result is shown in Fig. 5.
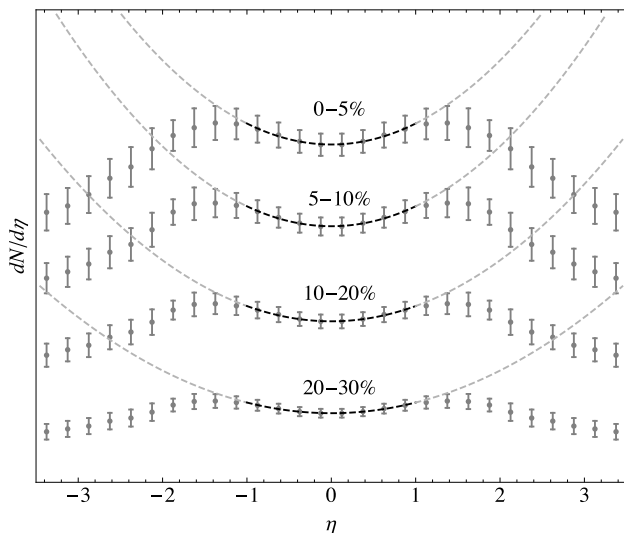
Class	a	b	b/a	χ^2/ndf
0-5%	1930	89	0.046	5.7×10^{-3}
5-10%	1584	84	0.053	4.6×10^{-3}
10-20%	1182	65	0.055	3.5×10^{-3}
20-30%	793	45	0.057	1.5×10^{-3}
40-50%	318	20	0.063	9.1×10^{-4}
60-70%	95	6.8	0.072	1.1×10^{-4}

Figure 5: Obtained fits for $Pb+Pb$ ($\sqrt{s_{\mathrm{NN}}} = 5.02$ TeV) charged particle η distributions for different centrality classes to data presented in [29]. Higher centrality classes are omitted from the figure.

The ratios between the constant basis a and the quadratic coefficient b lie around 0.06, with a slight centrality-class dependence. We therefore adopt the distribution function

$$\frac{dN_D}{d\eta} = 1 + \frac{a}{b}\eta^2, \quad \eta \in [-0.8, 0.8], \quad (11)$$

in which a/b corresponds to the fit-obtained value for each centrality class. The range specified is smaller than the actual detector range because D mesons can only be reconstructed for original trajectories that obey $|\eta| \lesssim 0.8$ due to the decay topology [15][8].

3.6 Transverse Momentum

It is standard practice to use lattice QCD (numerical evaluation of non-pertubative quantum chromodynamics) to predict heavy-flavour quark production in high-energy particle collisions, for instance using the FONLL framework [30]. For the purpose of this simulation however, we prefer to work with an analytical spectrum. In earlier work, succesful attempts have been made at describing charged particle p_{T} distributions by means of Tsallis thermostatistics, which is based on a generalisation of the better-known Boltzmann-Gibs statistics [31]. The relevant distribution function that holds around mid-rapidity is given by

$$\frac{dN}{dp_{\mathrm{T}}} = p_{\mathrm{T}} m_{\mathrm{T}} \cdot \left(1 + \frac{(q-1)m_{\mathrm{T}}}{T_q}\right)^{-\frac{q}{q-1}}, \quad (12)$$

in which m_{T} denotes the transverse mass

$$m_{\mathrm{T}} \equiv \sqrt{p_{\mathrm{T}}^2 + m^2}. \quad (13)$$

The parameters q and T_q represent the Tsallis-thermostatistics-specific q-factor and q-Temperature, the latter being defined as the derivative of the energy with respect to the Tsallis entropy

$$S_q \equiv \frac{k_B}{1-q}\left(1 - \sum_i p_i^q\right), \quad (14)$$

from which the Boltzmann-Gibs entropy is recovered in the limit $q \to 1$ [32].

The distribution shown in Eq. 12 was fitted to ALICE, CMS and ATLAS $p + p$ charged particle data samples at center-of-momentum energies $\sqrt{s_{\mathrm{NN}}}$ of 0.9 - 7 TeV. The results obtained project a q-factor of 1.15 and a q-Temperature T_q of 75 MeV/k_B for $\sqrt{s_{\mathrm{NN}}} = 5.02$ TeV [31].

Even though the fit values were not obtained from D-meson spectra, we can obtain a projection by setting the mass m to the D^X-meson mass, averaged over the produced D-meson species. We perform a weighted averaging procedure over $N_{\mathrm{D,prompt}}^{\mathrm{RAW}}$ data presented in [33] for $Pb + Pb$ collisions at $\sqrt{s_{\mathrm{NN}}} = 2.76$ TeV and obtain an average mass $m_{\mathrm{D^x}}$ of 1882.0 ± 4.9 GeV/c². We assume that the ratios between the different D-meson species remain invariant under the increase in collision energy from $\sqrt{s_{\mathrm{NN}}} = 2.76$ to $\sqrt{s_{\mathrm{NN}}} = 5.02$ TeV.

The shape of $p+p$ and $Pb+Pb$ charged particle p_{T} spectra are not identical, however, due to p_{T}-dependent supression phenomena inside the QGP medium. This difference between $p+p$ and $Pb+Pb$

---

[8]To be specific, this range is p_{T}-dependent and is smaller for low-p_{T} [15]. We ignore this within the scope of this thesis.

spectra at the same $\sqrt{s_{\mathrm{NN}}}$ is defined in terms of the nuclear modification factor [34]

$$R_{\mathrm{AA}}(p_{\mathrm{T}}) = \frac{1}{\langle N_{\mathrm{coll}} \rangle} \cdot \frac{dN_{\mathrm{AA}}/dp_{\mathrm{T}}}{dN_{\mathrm{pp}}/dp_{\mathrm{T}}}, \qquad (15)$$

in which the scaling factor N_{coll} is the aforementioned number of binary (nucleon-nucleon) collisions in an $A + A$ heavy-ion collision, obtainable via Glauber Monte Carlo simulations (see Section 2.3). Since the size of the QGP depends heavily on the impact parameter, $R_{\mathrm{AA}}(p_{\mathrm{T}})$ is centrality-class dependent.
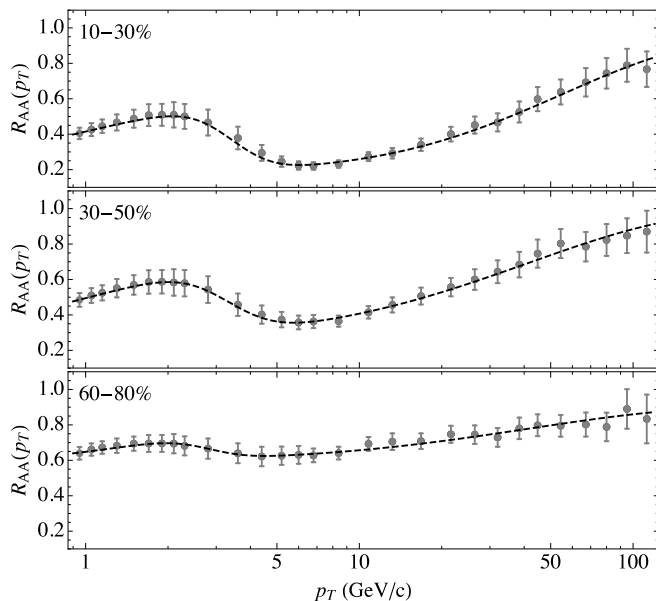
Class	$\langle R_{\mathbf{AA}} \rangle$	$p_{\mathbf{T,min}}$	$\chi^2/\mathbf{ndf}$
10-30%	0.325	6.05	1.5×10^{-3}
30-50%	0.470	5.75	2.8×10^{-3}
60-80%	0.678	4.51	7.9×10^{-3}

Figure 6: Obtained fits for $Pb+Pb$ ($\sqrt{s_{\mathrm{NN}}} = 5.02$ TeV) charged particle $R_{\mathrm{AA}}(p_{\mathrm{T}})$ distributions for different centrality classes to data presented in [35]. $\langle R_{\mathrm{AA}} \rangle$ represents the average value for $1 < p_{\mathrm{T}} < 25$, the maximum supression occurs for $p_{\mathrm{T,min}}$.

The nuclear modification factors for D mesons have not yet been measured accurately. However, a sufficiently detailed description of $R_{\mathrm{AA}}(p_{\mathrm{T}})$ for $Pb+Pb$ collisions at $\sqrt{s_{\mathrm{NN}}} = 5.02$ TeV is available for the entire charged particle population [35]. For the purpose of our simulations, we assume this result extends to the D-meson distributions as this is a topic of ongoing research.

In order to obtain a usable anlytical description, we fit the data presented in [35] with an ad-hoc function consisting of a constant base, one normal distribution and one skewed normal distribution that both take $\log p_{\mathrm{T}}$ as an argument. The

results for the centrality classes relevant to our simulation are displayed in Fig. 6. In order to obtain $R_{\mathrm{AA}}(p_{\mathrm{T}})$ for 60-80% centrality, we average the values for 50-70% and 70-90% centrality.

Our final p_{T} spectra are constructed through a multiplication of the Tsallis distribution with the aforementioned parameter values (see Eq. 12) and the obtained analytical descriptions of the nuclear modification factor $R_{\mathrm{AA}}(p_{\mathrm{T}})$. We compare them to reconstructed D-meson p_{T} spectra from a 2015 $Pb + Pb$ $\sqrt{s_{\mathrm{NN}}} = 5.02$ TeV data sample in Fig. 7 and find them to be in sufficient agreement.

After a D meson has been assigned a transverse momentum it is either accepted into the data sample or rejected entirely based on the ALICE detector combined acceptance and efficiency characteristics ($Acc \times \epsilon$), in order to simulate the detection process. $Acc \times \epsilon$ values indicate the particle survival rate and lie in the 0 to 1 range. For instance, if the p_{T} interval to which the D meson belongs has an associated $Acc \times \epsilon$ value of 0.002, it has a 0.2% chance of making it into the dataset. $Acc \times \epsilon$ profiles for prompt D mesons in the relevant centrality classes are displayed in Fig. 8. Since the p_{T} spectra attain their maximum in the region where the $Acc \times \epsilon$ profiles are at their minimum, the overwhelming majority of D mesons are rejected from the final dataset.

3.7   Events and Multiplicity

By the end of LHC Run 2, the total number of ALICE $\sqrt{s_{\mathrm{NN}}} = 5.02$ TeV $Pb + Pb$ collisions (N_{events}) in each of our three centrality classes wil amount to 7.2×10^7. By the end of Run 3, this number might have increased tenfold, although this remains a projection at this point. We run our SIM1 toy Monte Carlo simulation for the full statistics of these runs.

In order to set our multiplicity parameter M, we turn to previous data analysis. A study of 3.2×10^6 0-20% central $\sqrt{s_{\mathrm{NN}}} = 2.76$ TeV collisions obtained a raw prompt D-meson yield ($N_{\mathrm{D,prompt}}^{\mathrm{RAW}}$) of $(3.84 \pm 0.34) \times 10^3$, when integrated over all D-meson species and p_{T} intervals [33]. In order to predict $N_{\mathrm{D,prompt}}^{\mathrm{RAW}}$ for $\sqrt{s_{\mathrm{NN}}} = 5.02$ TeV collisions, we use two p_{T}-integrated FONLL calculations to obtain an appropriate scaling factor by comparing total cross sections, which we determine at 1.499 (see Appendix C). After a subsequent scaling from 0-20% to 10-30% centrality via the average number of binary collisions $\langle N_{\mathrm{coll}} \rangle$, we obtain a projected raw prompt D-meson yield of $(8.0 \pm 0.7) \times 10^4$ for Run 2 (for 10-30% centrality). Based on numerical integration of our analytical p_{T} spectra, combined with the ALICE detector $Acc \times \epsilon$ profiles, we expect our simulation to reproduce these yields when M is set to 0.859. Other values for M can again be obtained via the appropriate scaling via the $\langle N_{\mathrm{coll}} \rangle$ associated with their centrality class, as obtained
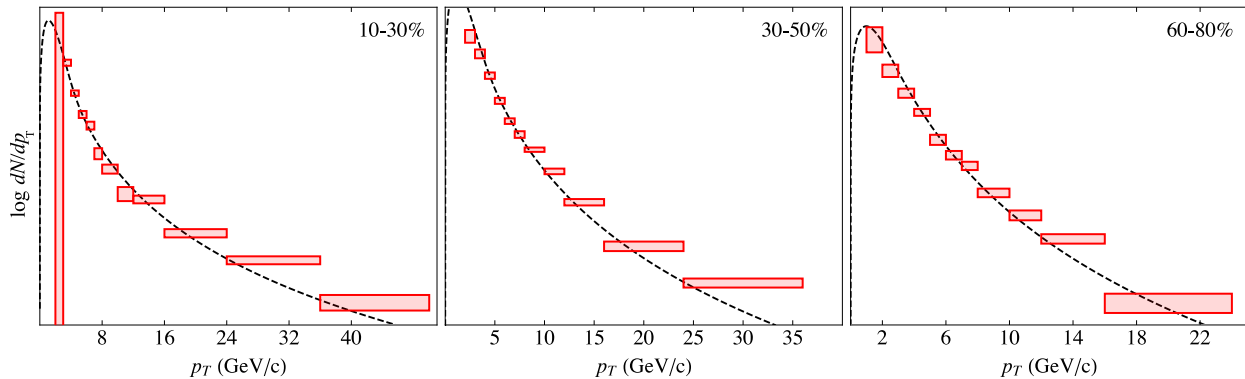
Figure 7: A comparison of our generated p_T spectra to reconstructed D-meson p_T spectra (binned) from a 2015 $Pb + Pb$ $\sqrt{s_{NN}}$ = 5.02 TeV data sample. The boxes represent the uncertainty in the bin-width-corrected volumes. *Data courtesy of the ALICE collaboration.*
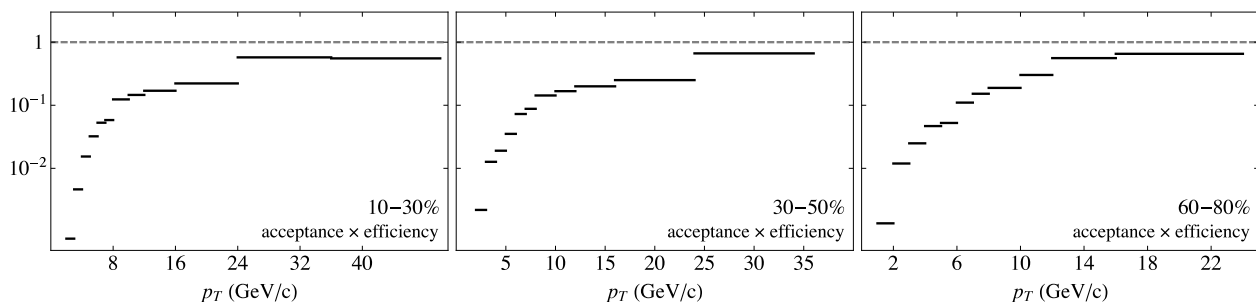

Figure 8: ALICE detector combined acceptance and efficiency ($Acc \times \epsilon$) profiles for prompt D mesons in the relevant centrality classes. *Data courtesy of the ALICE collaboration.*

via Glauber Monte Carlo simulations [19]. The resulting input variables for our toy Monte Carlo simulations are presented in Table 4. It must be noted that our simulation only takes integer input values for M. We can succesfully implement these floating-point values by inceasing M by a factor 10^3, as long as we simultaneously reduce N_{events} by the same order of magnitude. This should not have a significant effect on the simulation outcome for large N_{events}.

We run SIM2 for various $N_{D,prompt}^{RAW}$ in a range that best shows the improvement of the statistics, based on SIM1 results. We are specifically interested in the $\langle N_{D,prompt}^{RAW} \rangle$ for which the directed flow becomes demonstrable with a statistical significance of 5σ. The resulting input variables are presented in Table 3. SIM2 is not progressive: every intermediate run starts at zero. This ensures that the runs within the same centrality class are not correlated.

Class	N_{max}	step	N_{total}
10-30%	2×10^6	2×10^5	1.1×10^7
30-50%	10^6	10^5	5.5×10^6
60-80%	5×10^5	5×10^4	2.75×10^6

Table 3: SIM2 $N_{D,prompt}^{RAW}$ ranges and step sizes for the three centrality classes. Also displayed is the total number of $N_{D,prompt}^{RAW}$ generated, integrated over all steps.

3.8 Directed-Flow Parameter

As outlined in Section 2.4, a previous study has predicted the directed-flow parameter v_1 due to the initial EM fields in the QGP after $Pb+Pb$ collisions with $\sqrt{s_{NN}}$ = 2.76 TeV to be

$$\frac{dv_1}{d\eta}\bigg|_{\eta=0} \simeq \pm 1.75 \times 10^{-2}, \tag{16}$$

by means of a numerical analysis [5]. The increase in beam energy from $\sqrt{s_{NN}}$ = 2.76 to 5.02 TeV however, also increases the rapidity of the spectating nucleons, which should result in an increase of the field strengths since the induced EM fields due to a point charge moving at constant velocity v obey

$$\vec{E}(\vec{r}) = -\frac{q}{4\pi\epsilon_0} \cdot \frac{\gamma}{(1 + v_r\gamma^2/c^2)^{3/2}}\vec{r},$$
$$\vec{B}(\vec{r}) = -\frac{\mu_0 q}{4\pi} \cdot \frac{\gamma}{|\vec{r}|^3(1 + v_r\gamma^2/c^2)^{3/2}} \cdot \vec{v} \times \vec{r}, \tag{17}$$

which scale proportionally with the Lorentz factor γ in the limit $v \to$ c [36]. The increase in field strengths at $\sqrt{s_{NN}}$ = 5.02 TeV should therefore be non-negligible. The effective lifetime of the fields however, would scale with γ^{-1} and the time-integrated effects of the fields might be similar as a result. How this would interplay with the formation

Class	$\langle N_{\mathbf{coll}} \rangle$	$\langle N_{\mathbf{spec}} \rangle$	M	$\epsilon_{\mathbf{\Psi RP}}$	$v_1(\eta)$	R2 Yield	R3 Yield
10-30%	739	193	0.859	10%	$\pm 1.09 \times 10^{-2}$	7.97×10^4	7.97×10^5
30-50%	246	309	0.286	10%	$\pm 1.74 \times 10^{-2}$	5.15×10^4	5.15×10^5
60-80%	26.7	393	0.031	15%	$\pm 2.21 \times 10^{-2}$	1.60×10^4	1.60×10^5

Table 4: Input variables for SIM1 and SIM2 for three centrality classes. The average number of binary (nucleon-nucleon) collisions $\langle N_{\mathrm{coll}} \rangle$ and average number of spectating nucleons $\langle N_{\mathrm{spec}} \rangle$ are obtained via Glauber Monte Carlo simulations [19]. Also presented are the expected Run 2 and Run 3 prompt D-meson yields, for the relevant $N_{\mathrm{events}} = 7.2 \times 10^7$ and 7.2×10^8.

time of the QGP constituents remains unknown at this point.

Furthermore, the analysis performed in [5] does not take the ALICE detector $Acc \times \epsilon$ profiles into account. This might also affect the magnitude and/or direction of the measured flow, as previous research has shown that whether the Hall or Faraday effect is dominant depends heavily on the individual particle transverse momenta [6]. An adjusted numerical simulation could generate a new p_{T}-integrated prediction or even a $v_1(\eta, p_{\mathrm{T}})$ relation, yet this also falls outside the current scope of this thesis.

Finally, at higher centralities the QGP is smaller in size, which might result in less kinetic relaxation of the CQ's while they traverse plasma. In that case, the observable directed flow should be larger. Aforementioned future numerical analysis should provide clarification about the extent to which this is the case.

As we leave these considerations to future study, we adopt the definition of $v_1(\eta)$ as presented in Eq. 16 for the purpose of our simulations. This prediction however, was calculated for an impact parameter b of 9.5 fm and v_1 might vary depending on the centrality class. Because the directed flow arises due to the movement of spectator nucleides and EM fields are additive, we scale $v_1(\eta)$ proportionally with $\langle N_{\mathrm{spec}} \rangle$[9]. The resulting values are presented in Table 4.

3.9 Centrality Classes

As is evident from the previous subsections, many of the simulation parameters and distribution functions are heavily centrality-class dependent. This constitutes our main motivation for performing the simulations across these different centralities. The most central (0-10%) centrality class is not taken into account since we do not expect significant directed flow to occur, due to the low $\langle N_{\mathrm{spec}} \rangle$.

The D-meson multiplicity decreases drastically for higher centrality classes, but the p_{T}-integrated $Acc \times \epsilon$ fraction increases simultaneously, leading to a weaker decrease in predicted $N_{\mathrm{D,prompt}}^{\mathrm{RAW}}$. Meanwhile, the magnitude of the directed-flow parameter $v_1(\eta)$ increases for higher centralities, yet the uncertainty in the determination of the reaction plane Ψ_{RP} also increases for the 60-80% centrality class, leading to a weakening of the measurable signal. Our simulations are therefore designed to take these features into account and determine which centrality class would be most effective in measuring a hypothetical directed flow.

4 Results

4.1 SIM1

We analyse the D-meson populations generated in SIM1 (according to the input parameter values displayed in Table 4) with respect to their azimuthal angle (ϕ) and rapidity (η) distributions, after they have been split into charm and anticharm populations. For each particle, $\cos(\phi - \Psi_{RP})$ is calculated and the values are stored in six η bins to obtain a tractable per-bin yield. An averaging procedure delivers a $\langle \cos(\phi - \Psi_{RP}) \rangle$ value for each η bin (including the statistical uncertainty), as in line with Eq. 5. The resulting $\langle \cos(\phi - \Psi_{RP}) \rangle(\eta)$ profiles for the full statistics of Runs 2 & 3 in the three centrality classes currently under consideration are presented in Fig. 9.

We perform a weighted linear fit (without constant base) to the charm and anticharm populations separately, of which the result is also presented in Fig. 9, including a 1σ confidence interval (dashed lines). We finally obtain the directed-flow coefficients $v_1(\eta)$ after a weighted averaging of the absolute slopes of said fits and the centrality-class-dependent correction for the reaction plane error (see Section 3.3).

A side-by-side comparison of the obtained $v_1(\eta)$ values for Runs 2 & 3 in the different centrality classes is presented in Fig. 10, along with the statistical significance of measured directed flow with respect to non-flow (i.e. $v_1(\eta) = 0$). A complete overview of all SIM1 results is presented in Table 5, including the relevant raw D-meson yields. For an overview of the obtained raw D-meson p_{T} spectra, we refer to Appendix B.

---

[9]We should note that at lower centralities, the initial boosting of the QGP along the z-axis would be stronger due to a higher inital energy density. We do not consider the effect this may have on the Hall current at this point.
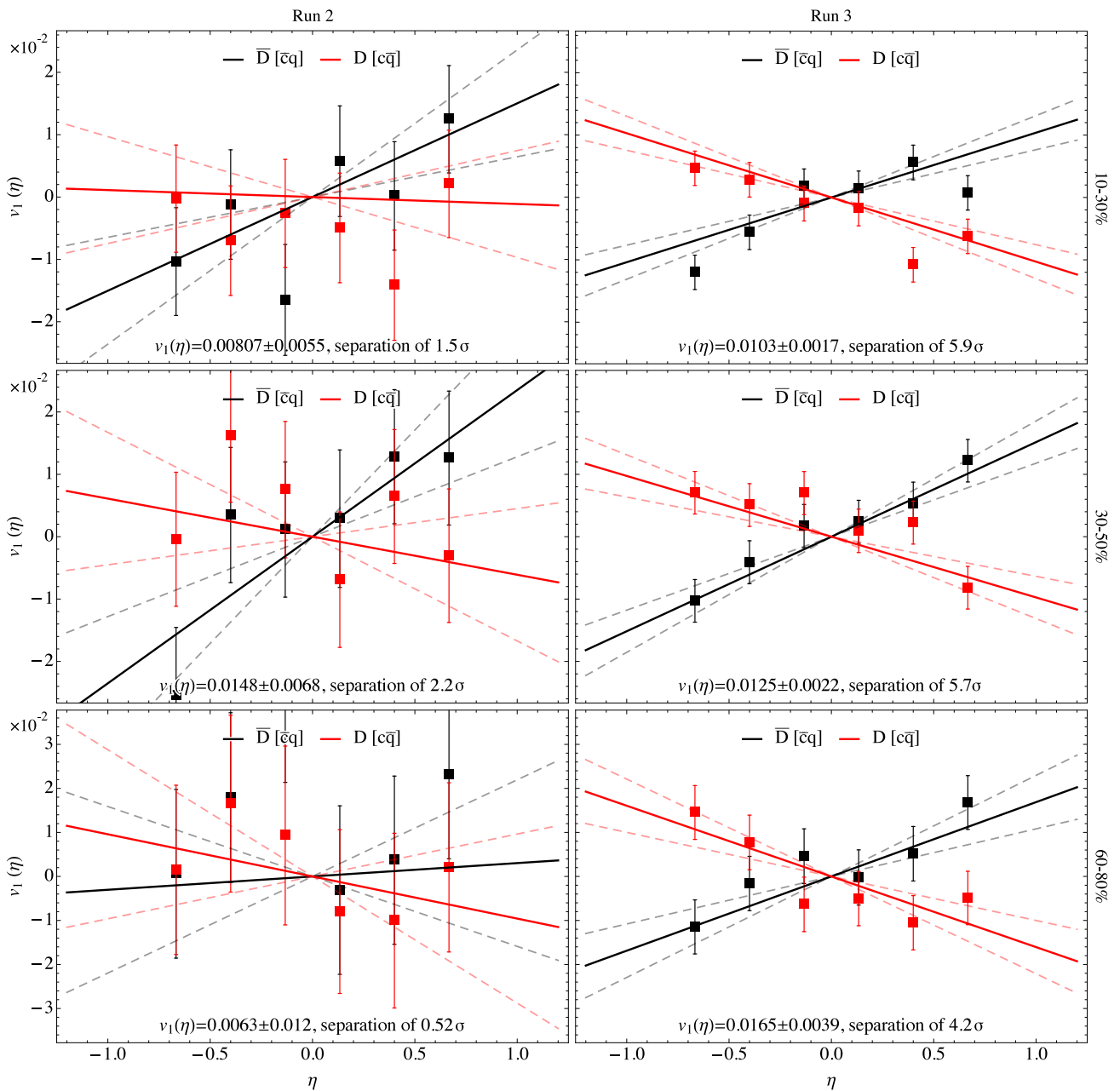
Figure 9: SIM1 projection of directed-flow reconstruction for ALICE $\sqrt{s_{NN}} = 5.02$ TeV $Pb + Pb$ D-meson data in three different centrality classes to be obtained in LHC Runs 2 & 3. The error bars represent 1σ confidence intervals.
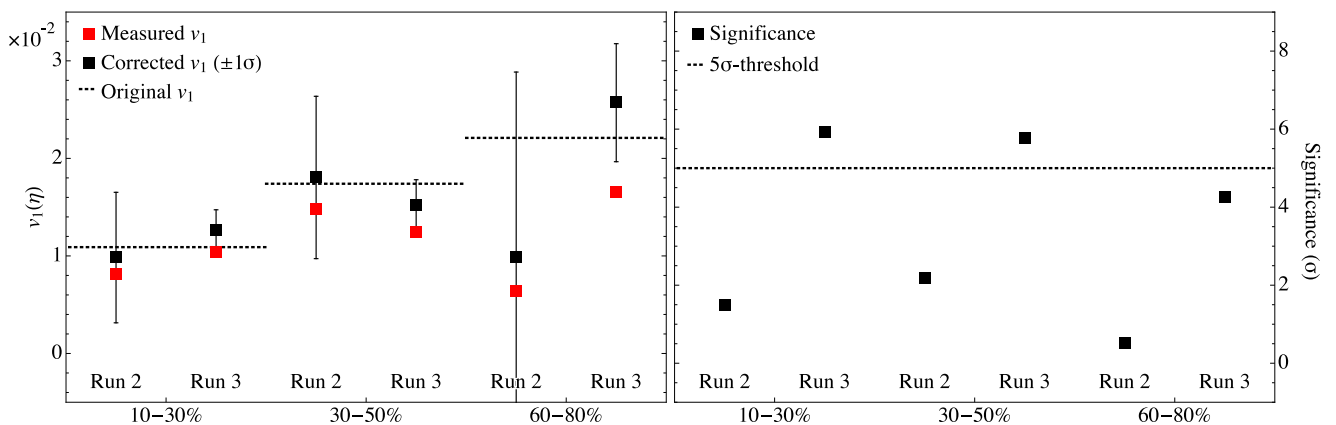

Figure 10: Side-by-side comparison of the statistics obtained in SIM1 for Runs 2 & 3 and three different centrality classes. The red squares represent the values before the reaction-plane-resolution correction.

Class	M	$v_1(\eta)_{\mathbf{input}}$	$v_1(\eta)_{\mathbf{measured}}$	$N_{\mathbf{D,prompt}}^{\mathbf{RAW}}$	Stat. Sign.
			Run 2		
10-30%	0.859	$\pm 1.09 \times 10^{-2}$	$(1.0 \pm 0.7) \times 10^{-2}$	78698	1.5σ
30-50%	0.286	$\pm 1.74 \times 10^{-2}$	$(1.8 \pm 0.8) \times 10^{-2}$	51001	2.2σ
60-80%	0.031	$\pm 2.21 \times 10^{-2}$	$(1.0 \pm 1.9) \times 10^{-2}$	15966	0.5σ
			Run 3		
10-30%	0.859	$\pm 1.09 \times 10^{-2}$	$(1.3 \pm 0.2) \times 10^{-2}$	783296	5.9σ
30-50%	0.286	$\pm 1.74 \times 10^{-2}$	$(1.52 \pm 0.26) \times 10^{-2}$	508380	5.7σ
60-80%	0.031	$\pm 2.21 \times 10^{-2}$	$(2.6 \pm 0.6) \times 10^{-2}$	157898	4.2σ

Table 5: An overview of SIM1 results including the reconstructed directed-flow parameter $v_1(\eta)$ (after event-plane-resolution correction), the significance of the measurement with respect to non-flow and raw prompt D-meson yields for Runs 2 & 3 in the relevant centrality classes.

4.2   SIM2

In SIM2, we first analyse the D-meson populations (generated according to the input parameter values displayed in Table 4 and the $N_{\mathrm{D,prompt}}^{\mathrm{RAW}}$-ranges displayed in Table 3) in the same way as we do in SIM1. As mentioned before, the p_{T} distributions and $Acc \times \epsilon$ profiles are this time left out of the equation. The obtained values for $v_1(\eta)$ are presented in the top row of Fig. 11, in a similar fashion as the SIM1 results in the left panel of Fig. 10. Note that the simulations do *not* describe the evolution of one simulation with $N_{\mathrm{D,prompt}}^{\mathrm{RAW}} = N_{\mathrm{max}}$: for every intermediate raw prompt D-meson yield a complete simulation is run, starting at $N_{\mathrm{D}} = 0$. Hence the obtained values that are presented in Fig. 11 are uncorrelated.

In the middle row of Fig. 11 we present the statistical significance of the measurements with respect to non-flow. The SIM1 results are also displayed in order to facilitate a comparison. Assuming that the measurement improves $\propto \sqrt{N}$, we fit the σ-values with a square-root function to achieve an analytical description of the improvement of the statistics. The residuals of these fits are displayed in the lower panels of Fig. 11. Note that these residuals emphatically do *not* represent the differences between the input v_1 and the reconstructed v_1: they are the difference between the σ-values and their fitted functions. This might seem unusual, but in this experiment we are not interested in the accuracy of the obtained v_1 measurement itself but rather the significance to which directed flow may be discerned from non-flow.

From the residuals we obtain a standard deviation of the σ-values which we employ to calculate a 1σ confidence interval for the $N_{\mathrm{D,prompt}}^{\mathrm{RAW}}$-value at which we project to pass the 5σ threshold for the demonstration of directed flow. We then use the Run 3 $N_{\mathrm{D,prompt}}^{\mathrm{RAW}}$-values from SIM1 to translate this into the number of events that would be required. The results are displayed in Table 6.

Class	$\mathbf{SD}(\sigma)$	$N_{\mathbf{D}}^{\mathbf{5\sigma}}(\times 10^5)$	$N_{\mathbf{E}}^{\mathbf{5\sigma}}(\times 10^8)$
10-30%	0.60 ± 0.14	$8.5^{+2.5}_{-2.2}$	$7.8^{+2.3}_{-2}$
30-50%	0.69 ± 0.16	$3.1^{+0.8}_{-0.7}$	$4.4^{+1.1}_{-0.9}$
60-80%	0.58 ± 0.10	$3.1^{+0.8}_{-0.7}$	13^{+4}_{-3}

Table 6: Required raw prompt D-meson yields and, consequently, number of total collision events required to demonstrate the existence of directed flow at a 5σ confidence level in the three different centrality classes, as projected by SIM2. Confidence intervals are specified at the 1σ level.

5   Discussion

The first thing we notice is that the raw prompt D-meson yields produced in SIM1 are in excellent agreement with the predictions obtained beforehand by means of numerical integration (compare Tables 4 & 5). Furthermore, SIM1 and SIM2 results are also in notable agreement, both with one another as well as the original $v_1(\eta)$ input values. In addition, the residuals of the fits to the SIM2 statistical significances with respect to non-flow agree with a 1σ standard deviation. This are indications that the random generators in our toy Monte Carlo are behaving as desired and hence our other results are also more likely to be trustworthy.

SIM1 gives us a first glimpse of what kind of statistics to expect after an analysis of all Run 2 and Run 3 data in the considered centrality classes. The Run 2 simulations do not provide a demonstration of directed flow to an appreciable statistical certainty, although in the 30-50% centrality class the 2σ threshold is breached. In the Run 3 simulation however, discovery-level confidence ($> 5\sigma$) is obtained for 10-30% and 30-50% centrality. Both confidence levels however, are too close to 5σ to rule out chance-based outliers, since the simulations are stochastic processes.

SIM2 provides us with a more robust description of the evolution in the statistics and predicts that
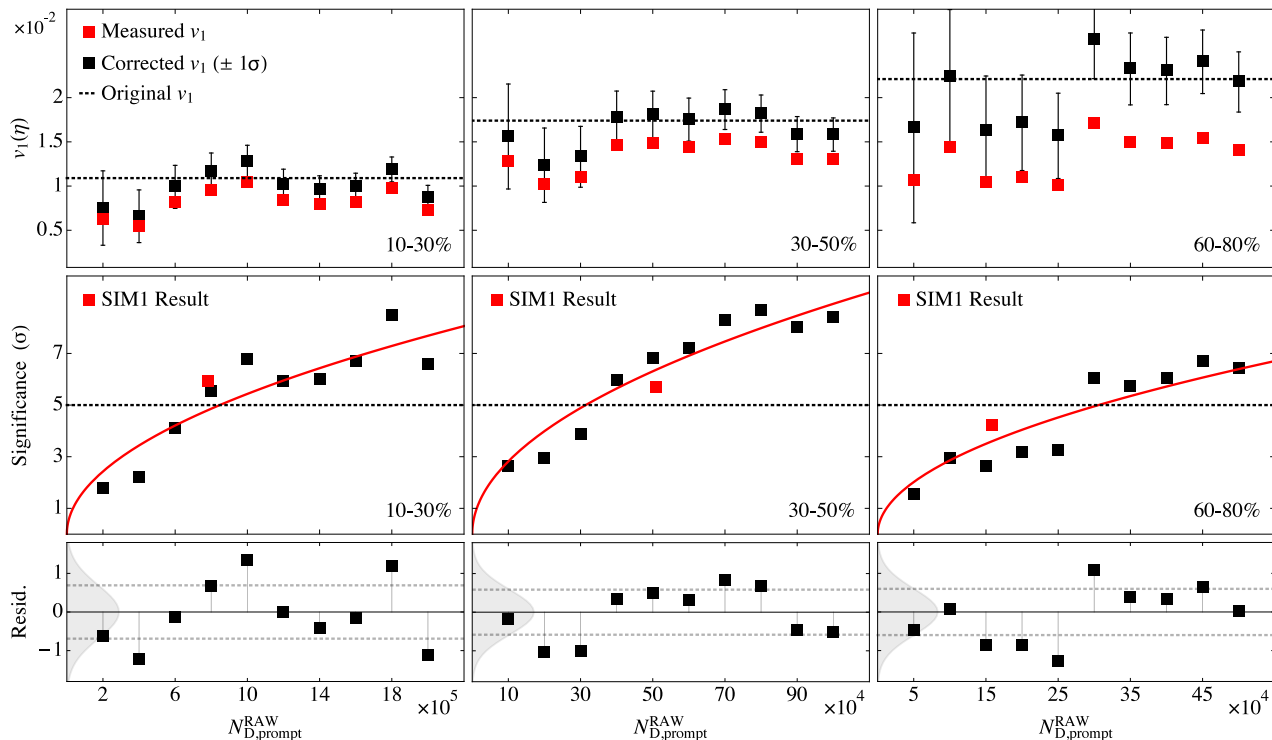
Figure 11: SIM2 projection of directed-flow reconstruction for ALICE $\sqrt{s_{NN}} = 5.02$ TeV $Pb + Pb$ collisions in three different centrality classes and a wide range of raw prompt D-meson yields $N_{D,prompt}^{RAW}$. **Top**: the reconstructed directed-flow coefficients $v_1(\eta)$. **Middle**: the statistical significance of the reconstructed directed flow with respect to non-flow, fitted with a square-root function. **Bottom**: the residuals of the aforementioned fit and their standard deviation (dashed).

$4.4^{+1.1}_{-0.9} \times 10^8$ collision events could be sufficient in order to demonstrate directed flow (of the magnitude simulated) in the 30-50% centrality class. The superiority of this class is not necessarily in line with what we observed in SIM1, in which 10-30% centrality provided a slightly better result. As we can see in the middle row of Fig. 11, this can be attributed to SIM1 incidentally overperforming at 10-30% centrality, while simultaneously underperforming at 30-50% centrality.

We have devised an analytical description of the projected confidence level to which current and future data samples of any size may be compared. If confidence levels at any time of observation lie below the curve, future expectations should be adjusted accordingly since LHC data is accumulated rather than analised separately, and hence present and future confidence levels are correlated.

Some interesting conclusions can be drawn from the difference in performance between the centrality classes. For 10-30% centrality, there is a much larger prompt D-meson multiplicity than for 30-50% centrality ($\sim \times 3$, see Table 4), but this is apparently offset by the decrease in magnitude of the directed flow and the smaller particle detection rates due to the $Acc \times \epsilon$ profile. For 60-80% centrality, both the magnitude of v_1 and the particle detection rates increase with respect to 30-50% centrality, but this effect is counteracted by not only the

decrease in multiplicity ($\sim \times 10^{-1}$), but also the increase in the reaction-plane-angle uncertainty. This is embodied by the fact that at 60-80% centrality a similar raw prompt D-meson yield is required to demonstrate a stronger directed flow, compared with 30-50% centrality. Our simulations show that when all of these effects are combined, the 30-50% centrality class emerges as the best candidate to demonstrate any hypothetical directed flow that is similarly centrality-class dependent.

A few matters need to be addressed in order to discuss the validity of our results. First of all, we have ignored the contribution of feed-down D mesons from B-meson decay to the prompt D-meson populations. As bottom quarks are less susceptible to the EM fields due to their mass and charge, this feed-down population should carry less directed flow and hence weaken the obtainable signal.

Secondly, we have scaled the magnitude of the directed flow linearly with $\langle N_{spec} \rangle$, without taking into account that at higher centralities the flow effect may be different, since less charm-quark kinetic relaxation will take place due to a smaller QGP. Neither did we take into account the effect which the stronger boosting due to inital QGP expansion may have on the sign and magnitude of the flow at lower centralities.

Furthermore, the directed flow is integrated over the initial prompt D-meson p_T spectra, instead of

over the obtainable raw prompt D-meson p_{T} spectra (after the application of the ALICE detector $Acc \times \epsilon$ profiles). As can be seen in Appendix B, these p_{T} distributions deviate from one another greatly, which could affect the sign and magnitude of the directed flow.

Finally, the numerical analysis performed in [5] is based on a per-nucleon-pair energy of 2.76 TeV instead of 5.02 TeV, while also assuming a constant QGP-conductivity σ_{el}. This is moderately unrealistic as σ_{el} is expected to be temperature-dependent. Both of these factors could also impact the sign and magnitude of the directed flow.

In order to improve our predictions, future research should focus on generating a new directed-flow prediction for each centrality class separately, while also taking all of the other aspects discussed into consideration. For the time being, however, our results provide a good first-order estimation of the measurability of any form of charge-dependent directed flow of the magnitude simulated.

6   Conclusions

Recent theoretical work has predicted the extreme magnitudes of the electromagnetic fields generated in non-central heavy-ion collisions, as well as the effect they may have on collision-produced D-meson populations in terms of directed flow. More insight regarding the strength and evolution of these fields will greatly assist in studying the quark-gluon plasma that is also produced in these collisions. We have performed two separate toy Monte Carlo simulations in order to predict the measurability of this directed flow for $\sqrt{s_{\mathrm{NN}}} = 5.02$ TeV $Pb + Pb$ collision data from the ALICE experiment that will be generated during LHC Runs 2 & 3.

We have based the relevant distribution functions on an extensive study of presently available $p + p$ and $Pb + Pb$ collision analyses and related theoretical models. Our simulations have been performed for the full (projected) statistics of LHC Runs 2 & 3 (SIM1), as well as a wider range of expected raw D-meson yields in their vicinity (SIM2).

Our results indicate that the 30-50% centrality class is best suited to demonstrate this directed flow, due to a combination of favourable conditions. By the end of Run 3, discovery-level confidence (5σ) should be attainable for this centrality class. In addition, we have obtained an analytical description of the evolution in this confidence level as a function of total number of collision events, to which any data sample may be compared.

Some simplifying assumptions have been made, however, both in calculating the theoretical directed flow, as well as during the construction of our simulations. Futhermore, there are some physics-related differences between the collisions used to generate this theoretical prediction and those on which we base our own simulations. This impacts the accuracy and potential validity of our projections. Hence, future research should focus on the impact on the directed flow that some of our assumptions may have, as well as calculating new directed-flow predictions more in line with the physics of actual ALICE $Pb - Pb$ collision data.

Nevertheless, our results provide a good first-order estimation of the measurability of any charge-dependent directed flow of the magnitude simulated. LHC Run 3 data from the ALICE experiment will therefore undoubtedly shed light on the electromagnetic fields generated in heavy-ion collisions, the properties of the quark-gluon plasma and therefore, perhaps, even the origins of our Universe itself.

References

[1] E. Shuryak, Soviet Physics - JETP **47:2**, 212 (1978).

[2] C. Chen, Nuclear Physics B - Proceedings Supplements **246-247**, 38 (2014), Proceedings of the 9th International Symposium on Cosmology and Particle Astrophysics.

[3] BRAHMS Collaboration, I. Arsene *et al.*, Nuclear Physics A **757**, 1 (2005), First Three Years of Operation of RHIC.

[4] H. Bohr and H. Nielsen, Nuclear Physics B **128**, 275 (1977).

[5] S. K. Das *et al.*, Physics Letters B **768**, 260 (2017).

[6] U. Gürsoy, D. Kharzeev, and K. Rajagopal, Phys. Rev. C **89**, 054905 (2014).

[7] CERN Scientific Policy Committee, The medium-term plan for the period 2018-2022 and draft budget of the organization for the sixty-fourth financial year 2018, 2017.

[8] E. M. Henley and A. Garcia, *Subatomic Physics*, 3 ed. (World Scientific, 2008).

[9] B. R. Martin, *Nuclear and Particle Physics*, 1 ed. (John Wiley & Sons, Ltd., 2006).

[10] Particle Data Group, C. Patrignani et al., Chinese Physics C **40**, 1 (2016).

[11] ALICE Collaboration, J. Adam et al., Phys. Rev. C **94**, 034903 (2016).

[12] H. Iida et al., Phys. Rev. **D88**, 094006 (2013), 1304.1807.

[13] M. Ruggieri, S. Plumari, F. Scardina, and V. Greco, Nuclear Physics A **941**, 201 (2015).

[14] F. Scardina, S. K. Das, V. Minissale, S. Plumari, and V. Greco, Phys. Rev. C **96**, 044905 (2017).

[15] ALICE Collaboration, B. Alessandro et al., Journal of Physics G: Nuclear and Particle Physics **32**, 1295 (2006).

[16] ALICE Collaboration, S. Acharya et al., Submitted to: JHEP (2018), 1804.09083.

[17] ALICE Collaboration, B. Abelev et al., Journal of High Energy Physics **2012**, 112 (2012).

[18] Mazzilli, Marianna, EPJ Web Conf. **129**, 00033 (2016).

[19] ALICE Collaboration, B. Abelev et al., Phys. Rev. **C88**, 044909 (2013), 1301.4361.

[20] S. Voloshin and Y. Zhang, Z. Phys. **C70**, 665 (1996), hep-ph/9407282.

[21] S. A. Voloshin, A. M. Poskanzer, and R. Snellings, Landolt-Bornstein **23**, 293 (2010), 0809.2949.

[22] R. Snellings, New J. Phys. **13**, 055008 (2011), 1102.3010.

[23] F. Becattini et al., The European Physical Journal C **75**, 406 (2015).

[24] The ALICE Off-line Project, AliPhysics Documentation, `http://alidoc.cern.ch/AliPhysics/master/`.

[25] The ALICE Off-line Project, runFlowAnalysisOnTheFly.C on GitHub, `https://github.com/alisw/AliPhysics/blob/master/PWGCF/FLOW/macros/runFlowAnalysisOnTheFly.C`.

[26] F. Hermsen, flowAnalysis on GitHub, `https://github.com/florishermsen/flowAnalysis`.

[27] F. Hermsen, flowAnalysis2 on GitHub, `https://github.com/florishermsen/flowAnalysis2`.

[28] ALICE Collaboration, B. Abelev et al., Int. J. Mod. Phys. **A29**, 1430044 (2014), 1402.4476.

[29] ALICE Collaboration, J. Adam et al., Phys. Lett. **B772**, 567 (2017), 1612.08966.

[30] M. Cacciari, M. Greco, and P. Nason, JHEP **05**, 007 (1998), hep-ph/9803400.

[31] M. D. Azmi and J. Cleymans, J. Phys. **G41**, 065001 (2014), 1401.4835.

[32] C. Tsallis, Journal of Statistical Physics **52**, 479 (1988).

[33] ALICE Collaboration, B. Abelev et al., JHEP **09**, 112 (2012), 1203.2160.

[34] X.-N. Wang, Phys. Rev. C **61**, 064910 (2000).

[35] CMS Collaboration, V. Khachatryan et al., Journal of High Energy Physics **2017**, 39 (2017).

[36] D. J. Griffiths, *Introduction to electrodynamics; 4th edition.* (Pearson, Boston, MA, 2013).

[37] M. Cacciari, M. Greco, and P. Nason, FONLL Heavy Quark Production, `http://www.lpthe.jussieu.fr/~cacciari/fonll/fonllform.html`.

A   Technical Appendix

Our toy Monte Carlo simulations are performed within the environment of CERN's own C/C++ ROOT Data Analysis Framework (6.10.8) and make use of the AliFlow package from AliPhysics [24]. The SIM1 programming code is a modification of and an expansion on the `runFlowAnalysisOnTheFly` (rFAOTF) macro from said AliFlow package [25], while SIM2 is a custom build.

The first modification we have implemented, is the transition from ROOT5 to ROOT6. The former works with a code interpreter (Cint), while the newer ROOT6 uses a *just-in-time* compiler (Cling), an expansion on the LLVM and Clang libraries. While ROOT5 accepts deviations from strict C++ programming grammar, Cling does not allow for this freedom. A transition from ROOT5 to ROOT6 therefore requires a restructuring of the rFAOTF-macro code as well as some additional minor adjustments.

The second type of modifications concern the implementation of the many different parameter distributions as described in Section 3, as well as the storage of the required histograms in the final dataset. This also requires changing some key classes from the AliFlow package (`AliFlowEventSimpleMakerOnTheFly` and `AliFlowAnalysisWithMCEventPlane`).

The third large change concerns splitting up the tasks executed in the `runFlowAnalysisOnTheFly` macro and recombining them within PROOF (Parallel ROOT Facility). This allows for multi-core parallelisation and greatly increases the computational speed, depending on the number of dedicated processing cores available.

The final adaptations concern a slight restructuring of the `AliFlowEventSimpleMakerOnTheFly` class and the closing of two memory leaks. Without these changes, a simulation of the full LHC Run 2 & 3 statistics woud have been unattainable. Both adaptations were performed in the following code fragment:

`AliFlowEventSimpleMakerOnTheFly.cxx`

```
205  for( Int_t p=0;p<iMult;p++)
206  {
207    AliFlowTrackSimple *pTrack = new AliFlowTrackSimple();
208    pTrack->SetPt(fPtSpectra->GetRandom());
209    if(fPtDependentV2 && !fUniformFluctuationsV2)
210    {
211      // v2(pt): for pt < fV2vsPtCutOff v2 increases linearly, for pt >= fV2vsPtCutOff v2 =
           ↪   fV2vsPtMax
212      (pTrack->Pt() < fV2vsPtCutOff ?
213        fPhiDistribution->SetParameter(2,pTrack->Pt()*fV2vsPtMax/fV2vsPtCutOff) :
214        fPhiDistribution->SetParameter(2,fV2vsPtMax)
215      );
216    } // end of if(fPtDependentV2)
217    pTrack->SetPhi(fPhiDistribution->GetRandom());
218    pTrack->SetEta(gRandom->Uniform(-1.,1.));
219    pTrack->SetCharge((gRandom->Integer(2)>0.5 ? 1 : -1));
220    // Check uniform acceptance:
221    if(!fUniformAcceptance && !this->AcceptPhi(pTrack)){continue;}
222    // Check pT efficiency:
223    if(!fUniformEfficiency && !this->AcceptPt(pTrack)){continue;}

         (...)
245    pEvent->AddTrack(pTrack);

         (...)
254  }
```

In lines 221 and 223, particles (`pTrack`) are either accepted into or rejected from the final dataset. If they are rejected, the current iteration of the `for` loop is terminated via the `continue` command. The `*ptrack` pointer however, is not deleted. This leads to a memory leak that floods the RAM long before full LHC Run 2 & 3 statistics can be simulated. Furthermore, the acceptance $\times$ efficiency selections are p_T-dependent only. The relevant parameter is set in line 208, yet computation-intensive actions are performed in lines 209 to 219. This leads to a considerable waste of computational power, especially if the $Acc \times \epsilon$ survival rate of the particles is small. Hence, restructuring the code leads to a siginificant decrease in simulation runtime.

All of the modifications outlined in this section can be viewed on GitHub [26], as well as the custom-created SIM2 macro [27]. Table 4 presents the decrease in simulation runtime after the changes we have implemented.

Code version	$N_{\mathbf{cores}}$	Processor	Runtime
Original macro	1	2.4 GHz Intel Core i5 (I5-4258U)	1.12×10^5 s
Restructured class	1	2.4 GHz Intel Core i5 (I5-4258U)	196 s
PROOF	2	2.4 GHz Intel Core i5 (I5-4258U)	97 s
PROOF	4	2.5 GHz Intel Core i5 (I5-2400S)	74 s

Table 7: Performance of different SIM1 code versions in a speed test (10-30% centrality, $N_{\mathrm{events}} = 100$k, $M = 100$). The extreme decrease in runtime is largely determined by the $Acc \times \epsilon$ particle survival rate.

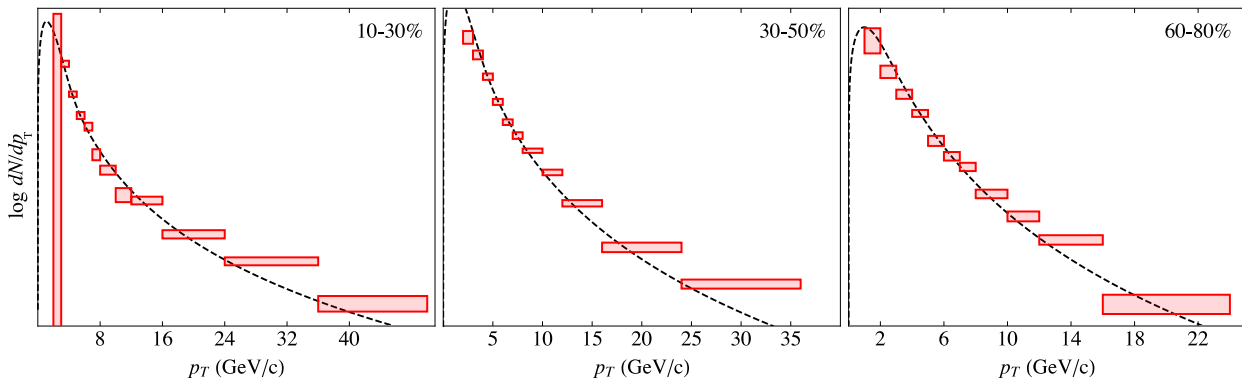# B   SIM1 Transverse Momentum Spectra

Figure 12: SIM1 input p_{T} distributions compared to reconstructed D-meson p_{T} spectra (binned) from a 2015 $Pb + Pb$ $\sqrt{s_{\mathrm{NN}}} = 5.02$ TeV data sample. The distributions are constructed from a combination of $\sqrt{s_{\mathrm{NN}}} = 5.02$ TeV $p + p$ spectra and the centrality-class-specific nuclear modification factors $R_{\mathrm{AA}}(p_{\mathrm{T}})$ (see Section 3.6). The boxes represent the uncertainty in the bin-width-corrected volumes. *Data courtesy of the ALICE collaboration. Figure identical to Fig. 7 in Section 3.6.*
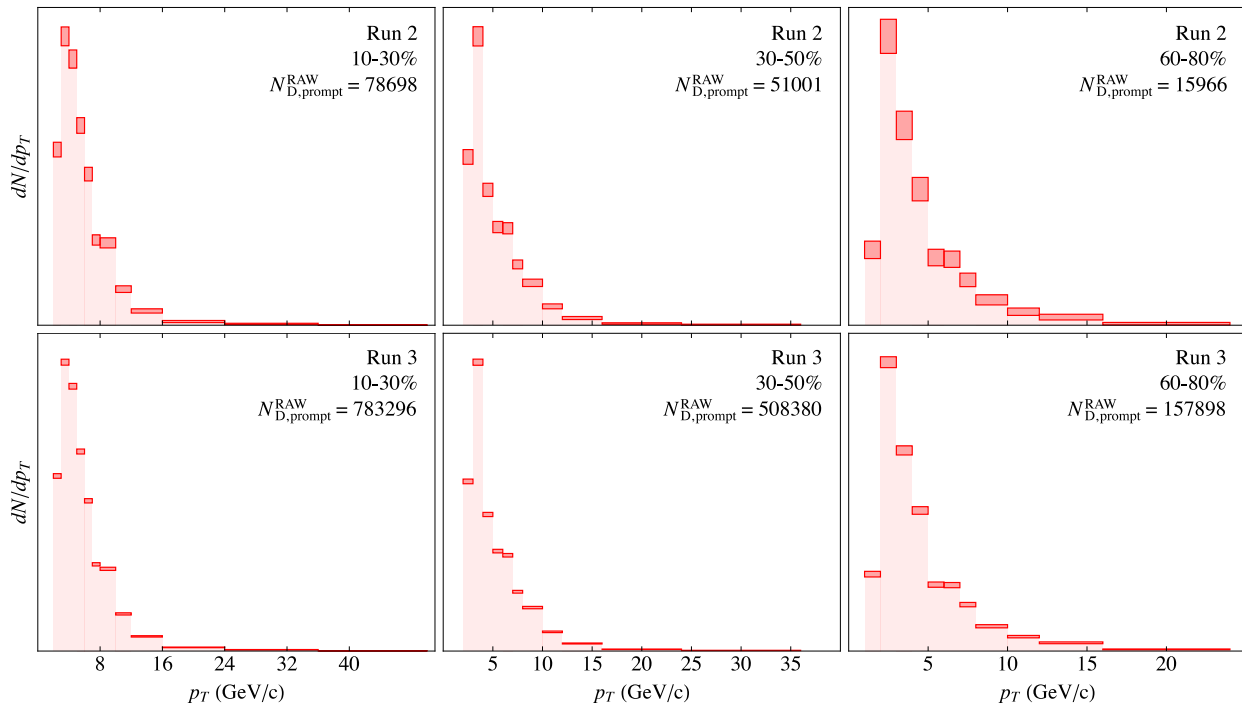

Figure 13: Raw D-meson p_{T} spectra obtained in SIM1 after the application of ALICE detector acceptance × efficiency profiles. The boxes represent the uncertainty in the bin-width-corrected volumes as obtained via $\sqrt{N}$. Note that in contrast to Fig. 12, the vertical axes are *not* logarithmic.

C   FONLL Calculations

As outlined in Section 3.7, we use two FONLL calculations to determine the difference in charged particle multiplicites between $Pb + Pb$ collisions of $\sqrt{s_{\mathrm{NN}}} = 2.76$ TeV and 5.02 TeV. The following output was generated, which also displays the input parameters [37].

$\sqrt{s_{\mathrm{NN}}} = 2.76$ TeV

```
1  # FONLL version and perturbative order: ## FONLL v1.3.2 fonll [ds/dpt^2dy (pb/GeV^2)]
2  # quark = charm
3  # final state = meson (meson = 0.7 D0 + 0.3 D+). NP params (cm,lm,hm) = 0.1, 0.06, 0.135
4  # BR(q->meson) = 1
5  # ebeam1 = 1375, ebeam2 = 1375
6  # PDF set = CTEQ6.6
7  # ptmin = 1
8  # ptmax = 50
9  # etamin = -0.8
10 # etamax = 0.8
11 # Uncertainties from scales
12 # cross section is sigma (pb)
13 # ptmin     central      min         max        min_sc      max_sc
14   1.0000 3.1680e+08 1.2480e+08 6.5230e+08 1.2480e+08 6.5230e+08
```

$\sqrt{s_{\mathrm{NN}}} = 5.02$ TeV

```
1  # FONLL version and perturbative order: ## FONLL v1.3.2 fonll [ds/dpt^2dy (pb/GeV^2)]
2  # quark = charm
3  # final state = meson (meson = 0.7 D0 + 0.3 D+). NP params (cm,lm,hm) = 0.1, 0.06, 0.135
4  # BR(q->meson) = 1
5  # ebeam1 = 2515, ebeam2 = 2515
6  # PDF set = CTEQ6.6
7  # ptmin = 1
8  # ptmax = 50
9  # etamin = -0.8
10 # etamax = 0.8
11 # Uncertainties from scales
12 # cross section is sigma (pb)
13 # ptmin     central      min         max        min_sc      max_sc
14   1.0000 4.7480e+08 1.6800e+08 9.7120e+08 1.6800e+08 9.7120e+08
```

A comparison of the generated total cross sections (central values) leads to the scaling factor of 1.499, which we employ to calculate the expected raw D-meson production at $\sqrt{s_{\mathrm{NN}}} = 5.02$ TeV.